Asymmetric vortex beam emission from a metasurface-integrated microring with broken conjugate symmetry

JIANZHI HUANG,[1,†] WANGKE YU,[1,†] HAILONG PI,[1] YIJIE SHEN,[2] ![ORCID] JIZE YAN,[1] AND XU FANG[1,*] ![ORCID]

[1]*School of Electronics and Computer Science, University of Southampton, Southampton SO17 1BJ, United Kingdom*

[2]*Optoelectronics Research Centre and Centre for Photonic Metamaterials, University of Southampton, Southampton SO17 1BJ, United Kingdom*

[†]These authors contributed equally to this work

[*]*x.fang@soton.ac.uk*

Abstract: Vortex beams that carry orbital angular moment (OAM) have recently attracted a great amount of research interest, and metasurfaces and planar microcavities have emerged as two prominent, but mostly separated, methods for Si chip-based vortex beam emission. In this work, we demonstrate in numerical simulation for the first time the hybridization of these two existing methods in a Si chip-based passive emitter (i.e., a light coupler). A unique feature of this device is its broken conjugate symmetry, which originates from introducing a metasurface phase gradient along a microring. The broken conjugate symmetry creates a new phenomenon that we refer to as asymmetric vortex beam emission. It allows two opposite input directions to generate two independent sets of OAM values, a capability that has never been reported before in Si chip-based passive emitters. In addition, we have also developed here a new analytical method to extract the OAM spectrum from a vector vortex beam. This analytical method will prove to be useful for vector vortex beam analysis, as mode purity analysis has rarely been reported in literature due to the complexity of the full-vector nature of such beams. This study provides new approaches for both the design and the analysis of integrated vortex beam emission, which could be utilized in many applications such as free-space optical communications and microfluidic particle manipulation.

1. Introduction

Optical metasurfaces are ultrathin layers of artificial nanostructures that enable a high level of control over the propagation of light [1]. Starting as a tool for manipulating freely propagating light, metasurfaces have subsequently been integrated with Si photonics platforms, in order to manipulate or transform optical modes confined in planar Si waveguides [2–5]. A typical demonstration is the generation of optical vortex beams [6], where a guided mode is converted into a freely propagating light wave that carries a finite value of orbital angular momentum (OAM) [7]. These meta-structured waveguides (or meta-waveguides [6]) are being intensively studied, due to the tremendous potential of vortex beams in applications such as particle manipulation [8] and free-space optical communications [9]. A shared feature of these OAM meta-waveguides is that they all utilize a non-circulating guided mode [10–16].

In parallel, microring emitters have emerged as another effective method to generate freely propagating OAM beams from a Si photonics chip [17–19]. This method has two crucial differences from the aforementioned meta-waveguide method: (1) it utilizes circulating whispering

gallery modes (WGMs) to twist the wavefront of the output light [20–24]; (2) it utilizes an angular grating where all the light scatterers are identical. By comparison, the guided mode in a meta-waveguide OAM emitter is non-circulating, and the device relies on a judiciously designed geometric variation (e.g., in size, shape or orientation) across its light scatterers (i.e., meta-atoms) for wavefront shaping [6].

In this work, we numerically demonstrate a new approach for integrated OAM generation, which hybridizes these two different methods. This is the first work that reports such hybridization in a passive device. In this approach, vortex beam emission is achieved by using a microring resonator that possesses a metasurface phase gradient. As compared to the two original design approaches, this hybrid approach allows for both wavelength-based OAM tuning (i.e., the output vortex beam changes its OAM value with wavelength) and geometry-based OAM tuning (with geometry referring to that of light scatterers, a gradient of which creates a gradient in the output phase). The former functionality is not available in the conventional meta-waveguides, while the latter represents a new concept to the regime of passive microring emitters.

A critical feature of this new design approach is symmetry breaking, which is created by the phase gradient. Symmetry breaking has profound importance in metasurface light manipulation. For example, a metasurface beam deflector can create a linear phase ramp that breaks the continuous rotational symmetry possessed by a planar surface. This symmetry breaking allows normal incident light to be deflected away from the surface normal [25,26]. Another example is the photonic bound states in the continuum (BIC). A BIC state has to be converted into a quasi-BIC state to facilitate its detection, and this often relies on breaking the geometric symmetry of the BIC metasurface [27,28]. A third example is to use metasurfaces to break the continuous rotational symmetry of a planar surface into discrete rotational symmetry that has a specific order. This has enabled a range of linear and nonlinear processes including vortex transmutation [29], nonlinear optical circular dichroism [30] and nonlinear wavefront control [31].

The meta-device proposed here breaks a form of conjugate symmetry. In free-space vortex beam generation, the conjugate symmetry is associated with the geometric phase and it forces right- and left-handed circular polarization to generate symmetric OAM values (i.e., values that are identical in absolute value but opposite in sign). Reference [32] reported for the first time a method based on metasurface J-plate to break the conjugate symmetry, which was subsequently used to develop OAM lasers [33]. For microring-based OAM emitters, the influence of the conjugate symmetry depends on whether the microring is an optically active device (i.e., a microring laser) or an optically passive device (i.e., a leaky waveguide antenna, the category that this work belongs to). In the former case, the conjugate symmetry again forces the OAM values to be symmetric. In order to generate nonzero net OAM, this symmetry must be broken, which has been realized through methods such as introducing to the microring cavity a metasurface [3], an externally applied non-Hermitian coupling [34], or a slight shape deformation [35]. By comparison, in the latter case where the microring contains no gain medium, the conjugate symmetry forces the OAM values to follow the direction of the WGM, which further follows the direction of input light [17]. In these waveguide couplers, launching light into a microring in the opposite direction only changes the helicity of the output light; it has no influence on the absolute value of the OAM.

As will be discussed in detail below, our device breaks the conjugate symmetry that constrains the OAM generation in conventional microring light couplers. It allows a single device to generate two independent sets of OAM values, which has never been reported before in Si chip-based emitters to the best of our knowledge. We refer to this type of OAM emission as asymmetric vortex beam emission. This phenomenon could be utilized in OAM multiplexing for high-capacity free-space optical communications [36,37]. Moreover, it allows for both wavelength-based and direction-based OAM tuning to function simultaneously. This feature

could be explored to generate highly scuplted electromagntic fields for manipulating particles and cells in miniaturized optofluidic systems [38–41].

In the analysis below, the generic device layout and the governing formula are first discussed in Section 2. It is followed by a discussion on the properties of individual meta-atoms in Section 3. An example device is then designed and analyzed in detail, and the analysis includes the properties of in-plane transmission (Section 4) and off-chip emission at two representative wavelengths (Sections 5 and 6). Section 6 also contains a new method for extracting an OAM spectrum from a vector vortex beam.

2. Design schematic of the emitter

Figure 1 schematically illustrates the proposed metasurface-integrated microring vortex beam emitter. The meta-device utilizes the silicon-on-insulator (SOI) platform, which is adopted in a plethora of areas including photonics crystals [42,43], metasurfaces [44,45], optomechanics [46,47], and photonic integrated circuits [48,49]. The meta-device consists of a Si microring resonator and a straight Si bus waveguide [Fig. 1(a)]. The microring is decorated on top with many uniformly distributed Si nanopillars, with a SiO_2 buffer layer inserted between the microring and the nanopillars. The nanopillars have a fixed height but vary in cross section, and together they function as a phase gradient metasurface. When the microring is driven at a resonance wavelength, a WGM forms inside the microring, which propagates either in the clockwise direction [Fig. 1(b), for input that propagates in the $+ x$ direction in the bus waveguide] or the counter-clockwise direction (for input in the -x direction). Through light scattering induced by the nanopillars, the metasurface extracts energy from the WGM and generates an OAM beam that propagates in the vertical direction (i.e., the $+ z$ direction) [Fig. 1(a)].

The meta-device possesses a metasurface-induced phase gradient [Fig. 1(b)]. In the conventional passive microring vortex beam emitters [17,20–24] that do not possess such a gradient, the topological charge l of the output vortex beam follows the angular phase-matching condition [17] and can be expressed as

$$l = \pm(m - q) \tag{1}$$

Here, m is the azimuthal order (i.e., the cycle number) of the WGM, and q is the element number of the angular grating (e.g., the number of holes in our recent work of Ref. [23]). The propagation direction (clockwise or counter-clockwise) of the WGM determines the sign of the topological charge but has no effect on its absolute value.

To modify Eq. (1) for the phase gradient microring shown in Fig. 1, we first interpret Eq. (1) by considering the phase difference α between adjacent light scatterers on a microring. For all passive microring OAM emitters, including both the conventional ones and the new type proposed here, the topological charge l of their OAM beam is always the number of optical cycles around the beam axis. By projecting these optical cycles onto the light source (i.e., the light scatterers along a microring), we can see that $l = q \cdot \alpha/(2\pi)$, where 2π represents the whole microring. By replacing a conventional angular grating (e.g., a set of identical holes in Ref. [23]) with a phase gradient metasurface [e.g., a set of different Si nanopillars as shown in Fig. 1(a)], we introduce a new contribution to the phase difference α. This new contribution is the intrinsic phase difference θ between adjacent nanopillars. Here, the term intrinsic implies that a phase difference can exist in light scattering, even if two nanopillars are excited at the same conditions, which is studied below in Fig. 2. We consequently can arrive at a generic expression for the topological charge l, which encompasses both the conventional passive microring emitters and the meta-devices studied here

$$l = \pm(m - q) + n \tag{2}$$

Here, $n = q \cdot \theta/(2\pi)$, and it is the contribution of the phase gradient metasurface. For a conventional microring emitter, $\theta = 0$ and Eq. (2) reduces to Eq. (1). The sign of n is independent
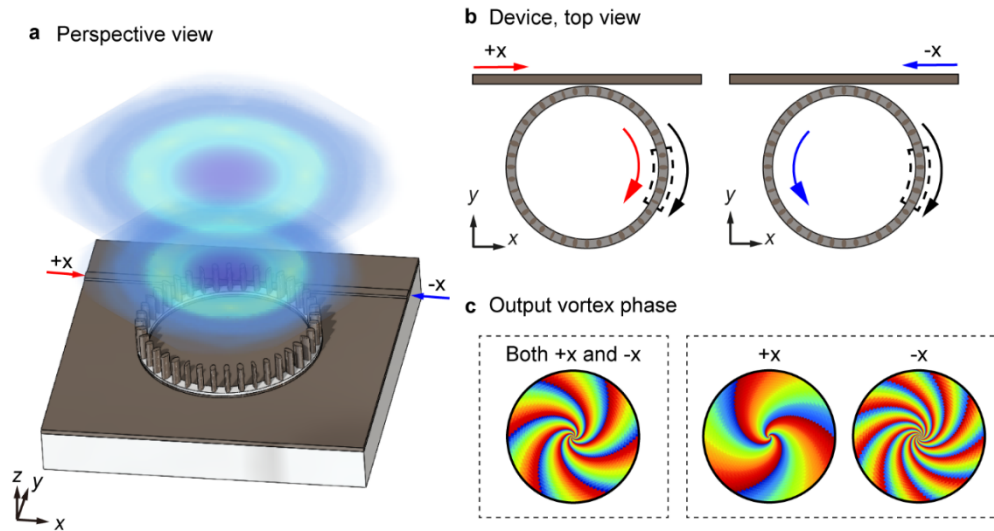
Fig. 1. Schematic diagram of the metasurface-integrated microring vortex beam emitter. (a) The emitter consists of a Si microring resonator evanescently coupled to a straight Si bus waveguide. A Si nanopillar-based phase gradient metasurface resides on top of the Si microring, and the metasurface and the microring are separated by a thin layer of SiO_2. The input light, which propagates in either the $+x$ or the $-x$ direction along the bus waveguide, can excite a WGM resonance inside the microring. The metasurface converts the WGM into a vertically propagating vortex beam that carries OAM. (b) The WGM can propagate in either the clockwise direction (the red curved arrow) or the counter-clockwise direction (the blue curved arrow), depending on the direction of the incident light. By comparison, the intrinsic phase gradient of a metasurface super unit cell (the black curved arrow and the dashed box) stays invariant. (c) The metasurface phase gradient breaks conjugate symmetry and generates a phenomenon that we refer to as asymmetric vortex beam emission. It allows the $+x$ and the $-x$ incident light to generate two independent sets of OAM values. Two possible output scenarios are illustrated here, where the two inputs, which have identical wavelength, can generate identical or very different output.

of the rotation direction of the WGM and the direction of the input light, because it originates from the intrinsic phase gradient of the metasurface [Fig. 1(b)].

The extra term n in Eq. (2) provides an extra degree of freedom for controlling the topological charge l in microring-based vortex beam emission. More importantly, it breaks the conjugate symmetry that exists in Eq. (1). Equation (1) forces l_{+x} and l_{-x}, the respective topological charge under the $+x$ and $-x$ input, to always follow $l_{+x} + l_{-x} = 0$. It implies that, flipping the input direction always results in flipping the helical wavefront of the vortex beam. By comparison, the new term of n in Eq. (2) does not change its sign with the input direction. This leads to $l_{+x} + l_{-x} \neq 0$, meaning that the conjugate symmetry between the $+x$ and $-x$ configurations is broken, for nonzero values of n. The values of l_{+x} and l_{-x} become independent of each other, because n is a parameter that can be adjusted independently from the value of $m - q$. We consequently refer to vortex beam emission that obeys $l_{+x} + l_{-x} = 0$ as symmetric vortex beam emission, and cases that follow $l_{+x} + l_{-x} \neq 0$ as asymmetric vortex beam emission. In the following sections, we numerically demonstrate the phenomenon of asymmetric vortex beam emission, by showing first a unique case where $l_{+x} = l_{-x} = -8$ (Section 5) and then a more general case where $l_{+x} = -9$ and $l_{-x} = -7$ (Section 6).
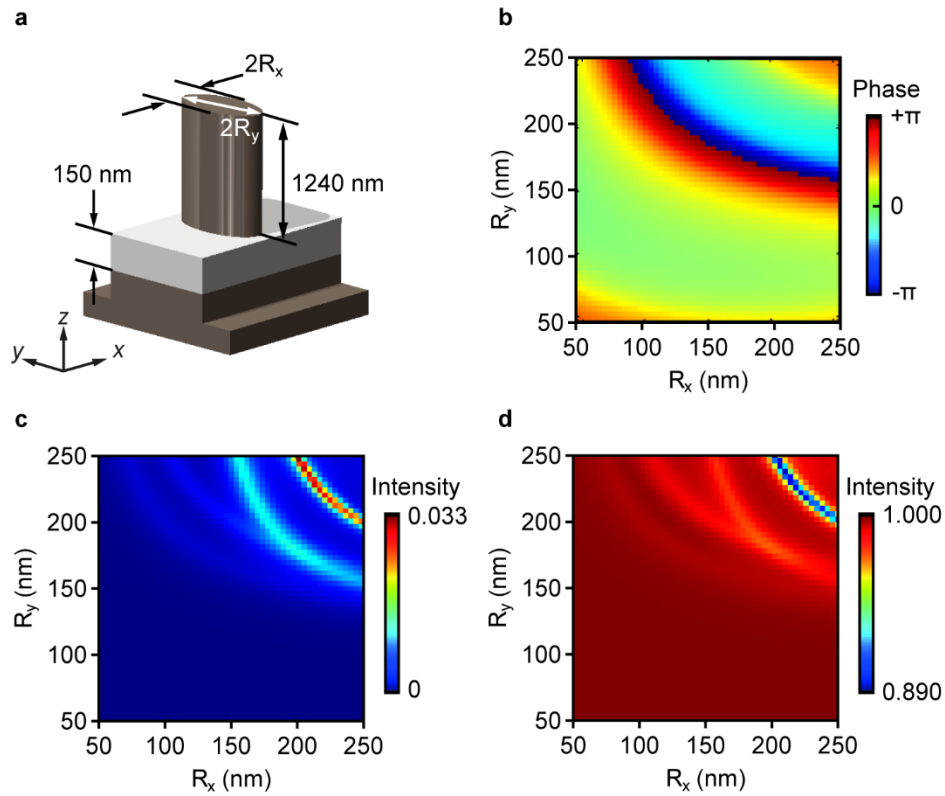
Fig. 2. Optical properties of individual meta-atoms. (a) Schematic of a meta-atom, which from the top consists of a Si nanopillar (1240 nm in height), a SiO_2 spacer layer (150 nm in thickness), and a Si rib waveguide (220 nm in core thickness and 100 nm for the rib). The whole meta-atom is on top of a SiO_2 buried oxide layer (not depicted). The schematic is not drawn to scale. (b-d) Optical properties simulated for a library of meta-atoms, with the free-space wavelength λ_0 taking a representative value of 1600 nm. All the meta-atoms have an elliptical cross section in the xy plane, and the principal semi-axis dimensions R_x and R_y are tuned from 50 to 250 nm at a step of 4 nm. (b) Phase of off-chip light scattering, normalized with respect to the phase of the input light. The values are taken at a height of approximately 2.5 μm above the center of the bottom surface of each nanopillar. (c) Corresponding intensity, normalized against that of the input light. The values are taken at the same height and from an integration window of 12 μm by 4 μm. (d) Residual intensity that remains confined in the waveguide, taken at the exit yz plane of the waveguide and normalized against that of the input.

3. Properties of individual meta-atoms

The metasurface is designed following a standard intuition-guided procedure [50], where a large number of different meta-atoms are characterized individually as the first step [Fig. (2)]. Figure 2(a) is the schematic of a single meta-atom, which consists of a Si nanopillar and a Si rib waveguide that are separated by a thin layer of SiO_2. The SiO_2 buffer layer is included here to suppress the strength of the evanescent coupling between the nanopillar and the waveguide [4,5]. Beneath the Si waveguide, a SiO_2 BOX (buried oxide) layer optically isolates the waveguide from the Si substrate [not depicted in Fig. 2(a)].

Figures 2(b)~2(d) show the numerically simulated electromagnetic properties of a large group of meta-atoms, covering the phase of the light scattered into free space [Fig. 2(b)], its intensity [Fig. 2(c)], and the intensity of the transmitted light that remains confined in the waveguide [Fig. 2(d)]. The simulation was conducted using a commercial finite-difference time-domain solver (FDTD solutions, Lumerical). Here, the free-space wavelength λ_0 of the input light was 1600 nm. As seen in Fig. 3 below, it was the peak wavelength of a WGM resonance, as well as the central wavelength of the whole spectrum investigated here (from 1550 nm to 1650 nm). The refractive indices of Si and SiO_2 were set as 3.476 and 1.444, respectively [51]. In each meta-atom, the rib Si waveguide had a core thickness of 220 nm, a core width of 500 nm, and a slab thickness of 100 nm [Fig. 2(a)]. The SiO_2 buffer layer above the core had a thickness of 150 nm, and the nanopillar further above had a height of 1240 nm. The waveguide was single mode, and the fundamental TE mode was used as the input for all the analysis in this work. All the nanopillars had an elliptical cross section in the xy plane, and they differed in their principal semi-axis dimensions R_x and R_y. One of the principal axes was always along the waveguide [i.e., the x axis in Fig. 2(a)], creating a mirror symmetry with respect to the vertical xz plane in all the meta-atoms. This mirror symmetry eliminated polarization rotation in the light scattering and simplified analysis. It is worth noting that, although the waveguide shown in Fig. 2(a) later constitutes a curved segment of a microring, it is treated as straight at this step of analysis. This is a good approximation, considering the large contrast in length between an individual meta-atom (0.63 μm) and the circumference of the microring (25.13 μm along its center).
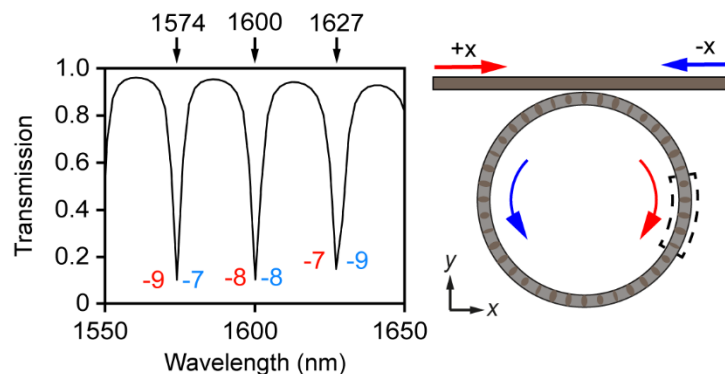

Fig. 3. Transmission of the example meta-device. The spectrum is independent of the input direction, which is along either +x or -x. Nevertheless, the OAM of the vortex beam is direction dependent. At the three resonance wavelengths of 1574, 1600 and 1627 nm, its value is -9, -8 and -7, respectively, under the +x input. Under the opposite input, the values are instead -7, -8 and -9.

The phase of the output light [Fig. 2(b)] is the most important parameter to consider in the metasurface design. Here, R_x and R_y are tuned independently from 50 to 250 nm at a step of 4 nm, creating a total of $51 \times 51 = 2601$ meta-atoms for selection. The phase values are taken at

approximately 2.5 µm above the bottom plane of the nanopillars. They are with respect to the input, which is launched into the waveguide 5 µm before the center of the meta-atom. The phase map possesses these three main features: (1) it provides the full 2π phase coverage; (2) it consists of multiple curved bands; (3) it is roughly symmetric with respect to the diagonal line that connects the smallest nanopillar ($R_x = R_y = 50$ nm) and the largest nanopillar ($R_x = R_y = 250$ nm). These features have been observed recently in Si nanopillars that are in direct contact with a strip waveguide [5]. We consequently can draw the same conclusion here, that the output phase seen in Fig. 2(b) is dominated by phase accumulated in propagation.

In addition to the output phase, the scattering intensity [Fig. 2(c)] and the residual intensity [Fig. 2(d)] are another two important parameters for meta-atom selection. Different from metasurfaces that function under the illumination of freely propagating light, the metasurface here is driven by a WGM, which can easily be disturbed by the light scattering of meta-atoms. For the results of Fig. 2(b) to serve as a good lookup table [50] to predict the device output wavefront, this disturbance has to be at a small level. To monitor this disturbance, we have simulated not only the output intensity of individual meta-atoms [Fig. 2(c)] but also the power that remains in the waveguide [Fig. 2(d)]. The values of the former are extracted at the same xy plane used for Fig. 2(b), by integrating the power outflow within a rectangular area of 12 µm by 4 µm. For the residual power shown in Fig. 2(d), the integration is conducted at the exit yz plane, which is 5 µm behind the central axis of the nanopillar.

Both Figs. 2(c) and 2(d) show that the nanopillar-induced mode perturbation is overall very weak. After normalization against the input power, slightly more than 95% nanopillars have a scattering intensity below 10^{-2} [Fig. 2(c)] and a residual intensity above 0.95 [Fig. 2(d)]. These nanopillars are considered to have a weak perturbation to the waveguide mode (consequently a weak perturbation to the WGM in a microring). This weak perturbation benefits from the use of the SiO_2 buffer layer, which can regulate the strength of the evanescent coupling between the Si waveguide and the Si nanopillars. Its thickness is chosen as 150 nm here, as a result of balancing the WGM mode integrity against the output intensity in the meta-device. The geometric dimensions and the optical properties of all the meta-atoms selected for the meta-device are listed in the Supplement 1.

4. In-plane transmission of the meta-device

Figure 3 shows the in-plane transmission of an example meta-device designed based on the results of the previous section. The meta-device has 40 nanopillars distributed uniformly along the microring. These 40 nanopillars are divided into eight repeating super unit cells, with each super unit cell containing five different nanopillars. The intrinsic phase difference θ between adjacent nanopillars is approximately $2\pi/5$, resulting in a linear phase ramp along the microring that takes the value of $n = -8$.

The transmission spectrum shown in Fig. 3 is invariant with incident direction, with the meta-device being a time-independent linear system that obeys the Lorentz reciprocity theorem. It features three sharp dips at 1574 nm, 1600 nm and 1627 nm. Each dip is associated with a WGM inside the microring. The values of the azimuthal order m are 41, 40 and 39, which are obtained by counting the optical cycles inside the microring. Note that the value of q in Eq. (1) is wavelength independent instead and stays as 40.

Interestingly, although they produce identical transmission spectra, the $+x$ incident light and the $-x$ incident light differ in their vertical emission. By using Eq. (2), the values of l_{+x} (i.e., the topological charge under the $+x$ incidence) and l_{-x} (i.e., that under the $-x$ incidence) are calculated for each WGM and specified in Fig. 3. For the resonances at 1574 nm, 1600 nm and 1627 nm, l_{+x} is -9, -8 and -7, respectively, while l_{-x} is -7, -8 and -9, respectively. Asymmetric emission, defined above as $l_{+x} + l_{-x} \neq 0$, is observed at all these three resonance wavelengths. It

is worth highlighting that, this result does not violate the Lorentz reciprocity theorem, because reversing the input direction here does not constitute a swap between input and output.

5. WGM and vortex beams at 1600 nm

In this section, we select one of the three WGM resonances, which has a free-space wavelength λ_0 of 1600 nm, and study it in detail (Fig. 4). Figures 4(a) and 4(b) show the field confinement of the bus waveguide and the microring. For both the $+x$ and the $-x$ input, most of the input light is coupled into the microring, building up a strong WGM resonance. Due to this strong coupling, the residual field that remains inside the bus waveguide behind the microring is very weak, which is congruent with the transmission dip seen in Fig. 3. We can see that Figs. 4(a) and 4(b) are almost mirror images of each other with respect to the vertical yz plane.
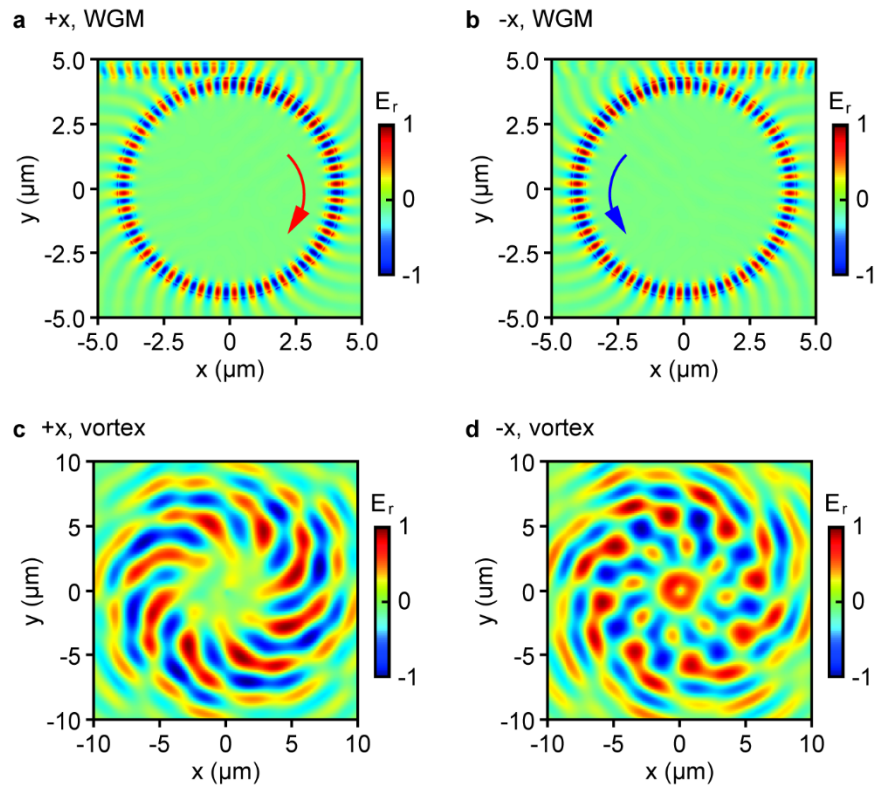

Fig. 4. Properties of the meta-device at a representative WGM resonance wavelength of 1600 nm. (a,b) The radially polarized electric field E_r inside the microring at (a) the $+x$ incidence and (b) the $-x$ incidence. The field is taken at the middle height of the Si waveguide. (c,d) The corresponding E_r field above the microring at (c) the $+x$ incidence and (d) the $-x$ incidence. The field is taken at 8 µm above the top of the Si waveguide. All the four panels are the top view. Each panel is normalized against its respective peak value.

Interestingly, the mirror symmetry of the near field [Figs. 4(a) and 4(b)] is not transferred to the emission into the far field [Figs. 4(c) and 4(d)]. Instead of being a pair of mirror images, the two output waves are closer to being identical copies. They both possess eight-fold rotational symmetry to a good degree, and for both of them the vortex spirals in the clockwise direction towards its center. This leads to $l_{+x} = l_{-x} = -8$. The sign here can also be verified by tracing the evolution of the electric field along the beam axis [21]. Relatively small differences exist between

Figs. 4(c) and 4(d), and they are attributed to factors such as small fluctuations in the output phase gradient and the output intensity among the meta-atoms. The device output efficiency, defined as the power ratio of the output vortex beam and the input guided mode, is 11.0% and 10.9% for the $+x$ and the $-x$ incidence, respectively. As most of the input light is coupled from the bus waveguide into the microring (Fig. 3), this efficiency is mostly limited by the efficiency of the near-field coupling between the microring and the metasurface, and the out-coupling efficiency of the metasurface.

This observation of $l_{+x} = l_{-x} = -8$ at 1600 nm can be interpreted by using Eq. (2). The order of the WGM inside the microring, which can be identified in Figs. 4(a) and 4(b), is identical to the number of nanopillars on top of the microring, i.e., $m = q = 40$, at this wavelength. Equation (2) consequently gives $l_{+x} = l_{-x} = n = -8$, which fits well with the numerical results shown in Fig. 4(c) and 4(d). Similar verification of Eq. (2) is also conducted for the two other WGM wavelengths (i.e., 1574 nm and 1627 nm), and the analytical results all fit with the numerical ones (see the Supplement 1 for details).

6. Vortex beam mode analysis

We notice that mode purity, a property critical for many potential applications such as free-space optical communications, is seldom analyzed in the literature on integrated OAM generation. The OAM beam emitted by the meta-device discussed here is a vector vortex beam. A vector vortex beam is a kind of structured light that possesses not only OAM but also spatially inhomogeneous states of polarization [52,53], and this full-vector feature makes mode purity analysis even more challenging. To provide insight on this challenge, we present in this section a method of mode purity analysis, and conduct calculation for the WGM wavelength of 1574 nm as an example (Fig. 5). The wavelength is changed from 1600 nm to 1574 nm here, because this wavelength possesses distinct values of l_{+x} and l_{-x}, making it a more rigorous test for our analytical method.

The first step of our method is to identify the dominant polarization component in the output. Figure 5(a) shows the output at one meter away from the meta-device (note that the distance here is not critical for the analysis, as long as it is in the far field that follows the paraxial approximation). Its intensity distribution has roughly a ring shape but lacks continuous rotational symmetry, which indicates that the OAM carried by the beam has a spectrum rather than a single value (an example of similar features can be found in the interference patterns shown in Ref. [7]). The polarization of the output changes in both ellipticity and direction with location. It is dominantly along the azimuthal direction at locations that bear significant intensity. As a reference, we have used the dipole modeling, where each meta-atoms is approximated with an infinitesimal electric dipole [23], to predict the ideal output beam, which is plotted in Fig. 5(b). The differences between Figs. 5(a) and 5(b) are attributed to the deviation of the meta-atoms from the ideal electric dipoles, which appear as a small but finite fluctuation in their output phase and the output strength (see the Supplement 1 for such fluctuations at 1600 nm).

As Fig. 5(a) reveals the existence of a single dominant field component, we can approximate the vector vortex beam with a scalar vortex beam. This scalar vortex beam retains the intensity distribution of the original vector vortex beam. Its spatial dependence of the phase is also the same as that of the azimuthal component in Fig. 5(b). It nevertheless has an identical state of polarization across the plane (hence a scalar vortex beam). This scalar vortex beam E can then be considered as a weighted superposition of the standard Laguerre-Gaussian modes $LG_l(r, \varphi)$

$$E = \sum_l C_l \, LG_l(r, \varphi) \tag{3}$$

where r and φ are the axial distance and the azimuthal angle of the cylindrical coordinate system, respectively. In this mode decomposition, only the Laguerre-Gaussian modes that have a zero radial index are considered [21], based on the intensity distribution of Fig. 5(a). Figure 5(c) shows
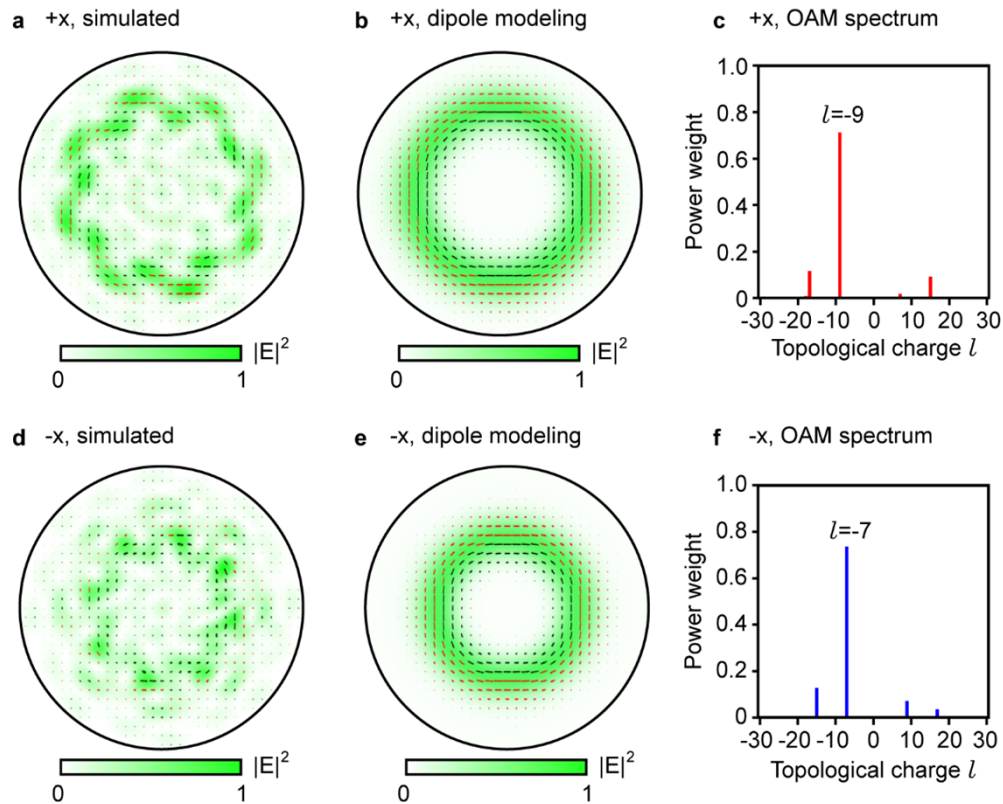
Fig. 5. Mode analysis for the output vortex beam. The wavelength is 1574 nm, another WGM resonance wavelength that is different from Fig. 4. (a) Intensity distribution of the output under the $+x$ incidence, overlaid with the polarization distribution. The map shows the hemisphere where every point is one meter away radially from the device. At locations that have a strong local intensity, the polarization is dominantly in the azimuthal direction. It can possess a small degree of ellipticity, which is expressed by using the red color (for the right-handed rotation, defined from the point of view of the receiver) and the black color (for the opposite handedness). (b) Corresponding intensity and field distribution for an ideal device, obtained by modelling all the meta-atoms as infinitesimal electric dipoles. (c) The OAM spectrum extracted from panel (a), utilizing only the azimuthal component of its electric field. (d-f) Corresponding results for the *-x* input, showing (d) the intensity and the polarization distribution of the meta-device, (e) the distributions of an ideal device, and (f) the OAM spectrum extracted from the azimuthal field of panel (d).

the spectrum of the weight $|C_l|^2$ for a broad range of l (equivalently l_{+x}, as the incident direction is $+x$ here) from -30 to 30. The dominant component is $l_{+x} = -9$, which has a weight of 71%. This mode analysis method is then applied on the output under the -x incidence [Fig. 5(d), with the ideal output also provided as Fig. 5(e) for comparison], and the extracted OAM spectrum is shown in Fig. 5(f). The dominant component is , which has a weight of 74%. Both the dominant l_{+x} and l_{-x} are the same as the analytical values predicted in Fig. 3. They are also consistent with the field distributions shown in the Supplement 1.

To further verify this method of OAM spectrum analysis, we deliberately pick a different component of the output electric field and repeat the analysis. The component used for the verification is the polar electric field, which is orthogonal to the azimuthal component used for Fig. 5. The OAM spectra obtained from the analysis can be found in the Supplement 1. Under the $+x$ incidence, $l_{+x} = -9$ is the dominant component and has a weight of 70%. Under the -x incidence, $l_{-x} = -7$ is the dominant component and has a weight of 74%. As compared to Fig. 5, this analysis produces identical values of the dominant l_{+x} and l_{-x}, as well as almost identical values of their weights. These results further verify the validity of our method.

Before concluding this work, it is worth discussing the use of the OAM spectrum analysis that we have developed here. In principle, the analysis can be applied to each constituent component of a vector vortex beam, as shown above. Nevertheless, these factors need to be considered when applying this analysis. (1) The dominant component will provide the highest numerical accuracy. (2) Information of both the intensity distribution and the polarization distribution is needed to identify the dominant component, as shown in Fig. 5. (3) Thanks to the linearity of Maxwell's equations, a vector vortex beam is allowed to carry different OAM values in its different constituent components. For such kind of complicated electromagnetic fields, our analysis will generate a set of distinct OAM spectra, each revealing a specific aspect of the original field.

7. Conclusion

To conclude, we have proposed and numerically demonstrated a new approach for integrated vortex beam emission. This new approach hybridizes two prominent existing approaches, which are based respectively on metasurface-structured waveguides and angular grating-decorated microrings. In the example device discussed in detail here, this approach is realized by positioning a Si pillar-based metasurface on top of a Si microring resonator. Because the metasurface phase gradient is intrinsic and does not switch with the direction of the input light, the conjugate symmetry that is intrinsic to the conventional microring emitters is broken here. The rotation direction of the source (i.e., the circulation of the WGM inside the microring) and that of the output (i.e., the helicity of the vortex beam) are no longer coupled. This is a new phenomenon that we refer to as asymmetric vortex beam emission. It allows for a single device to produce two independent sets of OAM values, with each value accessible via a unique combination of wavelength and input direction. This feature represents a new capability for integrated OAM emission.

In addition to demonstrating this new design approach, we have also developed here a new analytical method, which allows for extraction of an OAM spectrum from a vector vortex beam. The method is based on approximating the vector vortex beam as a scalar vortex beam, and subsequently using this scalar vortex beam to conduct mode decomposition. The results match well with both the analytical prediction and the simulated field maps. We believe both the hybridized design approach and the OAM spectrum analysis method presented here could significantly benefit future study on integrated vortex beam emission.

Data availability. Data underlying the results presented in this paper are available in Ref. [54].

Supplemental document. See Supplement 1 for supporting content.

References

1. F. Ding, A. Pors, and S. I. Bozhevolnyi, "Gradient metasurfaces: a review of fundamentals and applications," Rep. Prog. Phys. **81**(2), 026401 (2018).
2. Z. Y. Li, M. H. Kim, C. Wang, *et al.*, "Controlling propagation and coupling of waveguide modes using phase-gradient metasurfaces," Nat. Nanotechnol. **12**(7), 675–683 (2017).
3. X. X. Guo, Y. M. Ding, X. Chen, *et al.*, "Molding free-space light with guided wave-driven metasurfaces," Sci. Adv. **6**(29), eabb4142 (2020).
4. P. Y. Hsieh, S. L. Fang, Y. S. Lin, *et al.*, "Integrated metasurfaces on silicon photonics for emission shaping and holographic projection," Nanophotonics **11**(21), 4687–4695 (2022).
5. S. Y. Chen, J. Z. Huang, S. Q. Yin, *et al.*, "Metasurfaces integrated with a single-mode waveguide array for off-chip wavefront shaping," Opt. Express **31**(10), 15876–15887 (2023).
6. Y. Meng, Y. Z. Chen, L. H. Lu, *et al.*, "Optical meta-waveguides for integrated photonics and beyond," Light: Sci. Appl. **10**(1), 235 (2021).
7. S. Franke-Arnold, L. Allen, and M. Padgett, "Advances in optical angular momentum," Laser Photonics Rev **2**(4), 299–313 (2008).
8. A. Kritzinger, A. Forbes, and P. B. C. Forbes, "Optical trapping and fluorescence control with vectorial structured light," Sci. Rep. **12**(1), 17690 (2022).
9. Z. S. Wan, Y. J. Shen, Z. Y. Wang, *et al.*, "Divergence-degenerate spatial multiplexing towards future ultrahigh capacity, low error-rate optical communications," Light: Sci. Appl. **11**(1), 144 (2022).
10. Z. W. Xie, T. Lei, F. Li, *et al.*, "Ultra-broadband on-chip twisted light emitter for optical communications," Light: Sci. Appl. **7**(4), 18001 (2018).
11. B. Fang, Z. Z. Wang, S. L. Gao, *et al.*, "Manipulating guided wave radiation with integrated geometric metasurface," Nanophotonics **11**(9), 1923–1930 (2022).
12. Y. L. Ha, Y. H. Guo, M. B. Pu, *et al.*, "Monolithic-Integrated Multiplexed Devices Based on Metasurface-Driven Guided Waves," Adv. Theory Simul. **4**(2), 2000239 (2021).
13. X. P. Cao, N. Zhou, S. Zheng, *et al.*, "Digitized subwavelength surface structure on silicon platform for wavelength-/polarization-/charge-diverse optical vortex generation," Nanophotonics **11**(20), 4551–4564 (2022).
14. A. D. White, L. G. Su, D. I. Shahar, *et al.*, "Inverse Design of Optical Vortex Beam Emitters," ACS Photonics **10**, 803–807 (2022).
15. J. T. Ji, Z. Z. Wang, J. C. Sun, *et al.*, "Metasurface-Enabled On-Chip Manipulation of Higher-Order Poincare Sphere Beams," Nano Lett. **23**(7), 2750–2757 (2023).
16. H. Q. Huang, A. C. Overvig, Y. Xu, *et al.*, "Leaky-wave metasurfaces for integrated photonics," Nat. Nanotechnol. **18**(6), 580–588 (2023).
17. X. L. Cai, J. W. Wang, M. J. Strain, *et al.*, "Integrated Compact Optical Vortex Beam Emitters," Science **338**(6105), 363–366 (2012).
18. J. C. Ni, C. Huang, L. M. Zhou, *et al.*, "Multidimensional phase singularities in nanophotonics," Science **374**(6566), eabj0039 (2021).
19. Z. F. Zhang, H. Q. Zhao, S. Wu, *et al.*, "Spin-orbit microlaser emitting in a four-dimensional Hilbert space," Nature **612**(7939), 246–251 (2022).
20. G. H. Yuan, S. Y. Cao, P. N. Zhang, *et al.*, "Achieving wide-range photonics applications based on a compact grating-assisted silicon micro-ring resonator," Optik **183**, 887–896 (2019).
21. H. L. Pi, T. Rahman, S. A. Boden, *et al.*, "Integrated vortex beam emitter in the THz frequency range: Design and simulation," APL Photonics **5**(7), 076102 (2020).
22. L. Massai, T. Schatteburg, J. P. Home, *et al.*, "Pure circularly polarized light emission from waveguide microring resonators," Appl. Phys. Lett. **121**(12), 121101 (2022).
23. H. L. Pi, W. K. Yu, J. Z. Yan, *et al.*, "Coherent generation of arbitrary first-order Poincare sphere beams on an Si chip," Opt. Express **30**(5), 7342–7355 (2022).
24. X. Y. Lu, M. K. Wang, F. Zhou, *et al.*, "Highly-twisted states of light from a high quality factor photonic crystal ring," Nat. Commun. **14**(1), 1119 (2023).
25. F. He, K. F. MacDonald, and X. Fang, "Continuous beam steering by coherent light-by-light control of dielectric metasurface phase gradient," Opt. Express **28**(20), 30107–30116 (2020).
26. Z. Li, C. W. Wan, C. J. Dai, *et al.*, "Actively Switchable Beam-Steering via Hydrophilic/Hydrophobic-Selective Design of Water-Immersed Metasurface," Adv. Opt. Mater. **9**(17), 2100297 (2021).
27. K. Koshelev, S. Lepeshov, M. K. Liu, *et al.*, "Asymmetric Metasurfaces with High-Q Resonances Governed by Bound States in the Continuum," Phys. Rev. Lett. **121**(19), 193903 (2018).

28. Y. Zhou, Z. H. Guo, X. Y. Zhao, *et al.*, "Dual-Quasi Bound States in the Continuum Enabled Plasmonic Metasurfaces," Adv. Opt. Mater. **10**(19), 2200965 (2022).

29. Y. C. Zhang, J. Gao, and X. D. Yang, "Optical Vortex Transmutation with Geometric Metasurfaces of Rotational Symmetry Breaking," Adv. Opt. Mater. **7**(22), 1901152 (2019).

30. Y. T. Tang, Z. G. Liu, J. H. Deng, *et al.*, "Nano-Kirigami Metasurface with Giant Nonlinear Optical Circular Dichroism," Laser Photonics Rev **14**(7), 2000085 (2020).

31. B. Y. Liu, B. Sain, B. Reineke, *et al.*, "Nonlinear Wavefront Control by Geometric-Phase Dielectric Metasurfaces: Influence of Mode Field and Rotational Symmetry," Adv. Opt. Mater. **8**(9), 1902050 (2020).

32. R. C. Devlin, A. Ambrosio, N. A. Rubin, *et al.*, "Arbitrary spin-to-orbital angular momentum conversion of light," Science **358**(6365), 896–901 (2017).

33. H. Sroor, Y. W. Huang, B. Sephton, *et al.*, "High-purity orbital angular momentum states from a visible metasurface laser," Nat. Photonics **14**(8), 498–503 (2020).

34. Z. F. Zhang, X. D. Qiao, B. Midya, *et al.*, "Tunable topological charge vortex microlaser," Science **368**(6492), 760–763 (2020).

35. Z. Qiao, Z. Y. Yuan, S. Zhu, *et al.*, "High orbital angular momentum lasing with tunable degree of chirality in a symmetry-broken microcavity," Optica **10**(7), 846–852 (2023).

36. A. E. Willner, Y. X. Ren, G. D. Xie, *et al.*, "Recent advances in high-capacity free-space optical and radio-frequency communications using orbital angular momentum multiplexing," Phil. Trans. R. Soc. A. **375**(2087), 20150439 (2017).

37. C. He, Y. J. Shen, and A. Forbes, "Towards higher-dimensional structured light," Light: Sci. Appl. **11**(1), 205 (2022).

38. D. L. Gao, W. Q. Ding, M. Nieto-Vesperinas, *et al.*, "Optical manipulation from the microscale to the nanoscale: fundamentals, advances and prospects," Light: Sci. Appl. **6**(9), e17039 (2017).

39. S. Q. Yin, F. He, W. Kubo, *et al.*, "Coherently tunable metalens tweezers for optofluidic particle routing," Opt. Express **28**(26), 38949–38959 (2020).

40. T. Y. Li, X. H. Xu, B. Y. Fu, *et al.*, "Integrating the optical tweezers and spanner onto an individual single-layer metasurface," Photon. Res. **9**(6), 1062–1068 (2021).

41. Z. Shen, Z. Y. Xiang, Z. Y. Wang, *et al.*, "Optical spanner for nanoparticle rotation with focused optical vortex generated through a Pancharatnam-Berry phase metalens," Appl. Opt. **60**(16), 4820–4826 (2021).

42. Z. S. Liu, X. Y. Zhou, X. H. Jia, *et al.*, "Visible light perovskite-coated photonic crystal surface-emitter on SOI," Semicond. Sci. Technol. **35**(7), 075019 (2020).

43. J. L. Liao, Y. Z. Tan, Y. Gao, *et al.*, "Giant anomalous self-steepening and temporal soliton compression in silicon photonic crystal waveguides," APL Photonics **6**(8), 086107 (2021).

44. C. N. Yao, Y. L. Wang, J. H. Zhang, *et al.*, "Dielectric Nanoaperture Metasurfaces in Silicon Waveguides for Efficient and Broadband Mode Conversion with an Ultrasmall Footprint," Adv. Opt. Mater. **8**(17), 2000529 (2020).

45. X. Zhang, J. Li, J. F. Donegan, *et al.*, "Constructive and destructive interference of Kerker-type scattering in an ultrathin silicon Huygens metasurface," Phys. Rev. Materials **4**(12), 125202 (2020).

46. J. H. Zhang, P. N. Ruano, X. Le-Roux, *et al.*, "Subwavelength Control of Photons and Phonons in Release-Free Silicon Optomechanical Resonators," ACS Photonics **9**(12), 3855–3862 (2022).

47. K. Pelka, G. Madiot, R. Braive, *et al.*, "Floquet Control of Optomechanical Bistability in Multimode Systems," Phys. Rev. Lett. **129**(12), 123603 (2022).

48. C. R. Huang, S. Bilodeau, T. F. de Lima, *et al.*, "Demonstration of scalable microring weight bank control for large-scale photonic integrated circuits," APL Photonics **5**(4), 040803 (2020).

49. C. Y. Lian, C. Vagionas, T. Alexoudi, *et al.*, "Photonic (computational) memories: tunable nanophotonics for data storage and computing," Nanophotonics **11**(17), 3823–3854 (2022).

50. S. So, J. Mun, J Park, *et al.*, "Revisiting the Design Strategies for Metasurfaces: Fundamental Physics, Optimization, and Beyond," Adv. Mater. (Weinheim, Ger.) **35**(43), 2206399 (2023).

51. E. D. Palik, *Handbook of optical constants of solids* (Academic press, 1998), Vol. 3.

52. H. Rubinsztein-Dunlop, A. Forbes, M. V. Berry, *et al.*, "Roadmap on structured light," J. Opt. **19**(1), 013001 (2017).

53. Y. J. Shen, X. J. Wang, Z. W. Xie, *et al.*, "Optical vortices 30 years on: OAM manipulation from topological charge to multiple singularities," Light: Sci. Appl. **8**(1), 90 (2019).

54. The University of Southampton's ePrints research repository http://eprints.soton.ac.uk/.